CrossMark

Microstructure and electrical conductivity of aluminium/steel bimetallic rods processed by severe plastic deformation

Yuanshen Qi[1,*], Rimma Lapovok[2], and Yuri Estrin[1,3,*]

[1] *Department of Materials Science and Engineering, Monash University, Clayton, VIC 3800, Australia*
[2] *Institute for Frontier Materials, Deakin University, Geelong Waurn Ponds Campus, Pigdons Road, Geelong, VIC 3216, Australia*
[3] *Laboratory of Hybrid Nanostructured Materials, NUST MISiS, Moscow 119490, Russia*

ABSTRACT

Equal-channel angular pressing (ECAP) was used to fabricate Al/steel bimetallic rod for potential application in overhead transmission conductors. Bimetallic rods consisted of an austenitic stainless steel 316L core and an Al alloy 6201 cladding layer. By means of ECAP processing at 175°C, increase of mechanical strength without loss of electrical conductivity was achieved for one particular rod geometry out of three geometries tested. X-ray diffraction and transmission electron microscopy were employed to analyse how the microstructure was influenced by the number of processing passes and the bimetallic rod geometry. The co-deformation mechanism of the bimetallic rod under ECAP and accelerated dynamic ageing of Al alloy 6201 were discussed based on the microstructure characterisation results.

Introduction

Architectured multicomponent materials are attracting growing attention due to the unique properties they can offer [1–7]. A broad range of multicomponent materials with various architectures from bimetallic to multi-layered and multi-filamentary ones have been developed or are currently under development. For example, bimetallic titanium-cladded steel plates fabricated by explosive bonding and rolling have been extensively used in petrochemical industry for decades [8]. More recently, nanostructured multi-layered copper and niobium plates fabricated by accumulative roll bonding (ARB) were proposed for potential use in nuclear power industry as materials with high tolerance to radiation damage [9]. In addition, mechanical processing techniques producing gradient structures having a fine-grained, hardened surface layer on a metallic part are cropping up [10–12]. These include, among others, such methods as surface mechanical attrition treatment (SMAT) [13], friction stir processing (FSP) [14], three-roll planetary milling [15], and high-pressure tube twisting [16].

Among the architectured materials considered, bimetallic rods and wires with concentric cladding/

Address correspondence to E-mail: yuanshen.qi@monash.edu; yuri.estrin@monash.edu

core arrangement are particularly attractive for applications in electrical power transmission. An efficient way to produce bimetallic rods and wires for electrical transmission applications by co-extrusion was developed in the 1970s. By that time, Cu clad Al wire was invented as a cheaper and lighter alternative to copper wires. Researchers found that an optimum combination of the die angle, the die friction, and the extrusion ratio are critical for achieving uniform deformation of bimetals by extrusion [17, 18]. Further investigation revealed that, beside the extrusion process parameters, the ratio of the flow stresses of the cladding and the core materials can also affect the co-deformation flow characteristics and interface bonding [19, 20]. In addition to the mechanical properties of the materials, the geometry—more specifically, the relative thickness and length of the cladding layer—is another factor that can affect the extruded products [21, 22]. Subsequent research in this area was focused on how to improve the interface bonding and promote the solid state interdiffusion between the cladding and core of a bimetallic rod [23].

Through these studies it became evident that by processing at elevated temperatures and post-processing heat treatment, the atom exchange between dissimilar components can be accelerated. However, this may cause concurrent grain coarsening, residual thermal stresses and, most importantly, the formation of intermetallic compounds. All these phenomena may have a detrimental effect on the mechanical strength and fatigue performance of the bimetallic materials [24]. Therefore, instead of thermal treatment, plastic deformation can be employed as a preferred way to form the bonding [25–27]. The imposed plastic deformation, particularly shear strain, can disrupt the oxide layers on the surface of the constituent metals, expose fresh metal surfaces and bring them into close contact, thus promoting metallurgical bonding and element intermixing. Furthermore, due to increased concentration of deformation-induced crystal lattice defects, the diffusivity is expected to be enhanced [28].

Recently, axisymmetric forward spiral extrusion and rotary swaging were demonstrated to be effective methods for successful fabrication of bimetallic rods [29, 30]. However, the main limitation of these two methods is that the core component is not plastically deformed, the strain distribution is inhomogeneous

and the overall strain is low [29–31]. To obtain a better bonding quality, imparting a larger strain on both cladding and core material is required. Equal-channel angular pressing (ECAP), which is arguably the most popular severe plastic deformation (SPD) technique, is seen as a promising method for attaining the desired high levels of strain. A number of studies have shown that ECAP gives rise to a better bonding strength than the traditional extrusion process [32–34]. Recently, it was found that the quality of the bonding can be further improved using appropriate interlayers between the core and the sheath [35]. As in the case of extruded bimetallic rods, the bonding strength of ECAP-processed ones can be influenced by the thickness of the cladding component [36, 37].

While preliminary findings suggest that the method has a great potential, the viability of ECAP as a technique for producing bimetallic rods and wires has yet to be explored. Specifically, the present study aims at shedding light on important aspects of fabrication of bimetallic rods by ECAP. First, the influence of the relative thickness of the cladding layer on the interface microstructure will be systematically assessed by high-resolution characterisation to verify the hypothesis that it is controlled by bimetallic rod geometry and the ECAP schedule. Second, we shall be looking into the effect of the number of ECAP passes on the mechanical properties and electrical conductivities of the product in relation to its microstructure. Third, instead of Al and Cu which have been extensively studied, a rarely studied yet very viable type of bimetallic couple—Al and steel—was chosen for this study. A potential practical application is in electrical power transmission conductors. In such a hybrid, steel adds to the strength of the wire and Al carries most of the current. In addition to the good bonding, microstructure refinement in both components is expected to occur, which should have a positive effect on the overall performance of the hybrid structure in terms of strength and electrical conductivity. It should be noted that even though bimetallic rods were produced in this study at laboratory scale, ECAP does have the capacity of processing wires for continuous industry-scale application [38, 39]. Therefore, the proposed design is believed to be feasible for manufacturing high-performance electrical conductors that would meet the growing need for more efficient power transmission.

Materials and methods

Material and processing

To meet the requirements for the potential engineering application, careful materials selection was carried out first. Rather than using some of the available high strength steels, a conventional austenitic stainless steel 316L was selected due to its following attributes: high corrosion resistance, good formability and, most importantly, its being non-ferromagnetic. In the conventional overhead electrical conductors, a magnetic field originates from the high carbon steel wire, which is a ferromagnetic material. The magnetic field interferes with the flow of the electrical current and causes extra power losses due to an increase in the effective electrical resistance of the aluminium conductor. Furthermore, the dissipated power also leads to an increase in the temperature of the electrical conductor and may cause fatal problems with its stability [40]. In contrast, the non-ferromagnetic properties of austenitic steels eliminate the magnetic loss and enhance the stability and reliability of the conductor [40, 41].

For the outer Al-based cladding layer, aluminium alloy AA6201 was chosen. This alloy is widely used owing to its good combination of strength and electrical conductivity [42–44]. Moreover, further improvement of the mechanical strength and electrical conductivity of this alloy was shown to be possible by severe plastic deformation (SPD) [44–47]. By imposing extreme deformation at elevated temperature, decomposition of solid solution and formation of nano-sized second-phase precipitates at the expense of solute atoms occur. This dynamic ageing provided by SPD processing was found to result in a microstructure characterised by ultrafine grain structure, nano-sized precipitates, very low content of alloying atoms in solid solution and absence of Guinier–Preston (GP) zones, which leads to a significant enhancement of the electrical conductivity and concurrent improvement of strength [44].

The chemical composition of austenitic stainless steel 316L and Al alloy AA6201 used in this study is shown in Table 1. The as-received AA6201 rods were in the peak ageing condition. Steel bars 3, 4 and 5 mm in diameter were produced. Correspondingly, AA6201 tube with inner diameter of 3, 4 and 5 mm and outer diameter of 10 mm were manufactured. The length of the bars and the tubes was 40 mm. Steel bars were inserted in the matching AA6201 tubes with shrink fit. In this way, bimetallic rods with three initial geometries were prepared. They had a steel core with diameter of 3, 4 or 5 mm encased in an outer AA6201 cladding layer with a thickness of 3.5, 3 and 2.5 mm, respectively. The dimensions were chosen in such a way that the outer diameter of the bimetallic rod was the same in all three cases, namely 10 mm.

Bimetallic rods underwent one or four passes of ECAP at 175°C. In the latter case, route B_C was followed. The channel angle was 90° and the corner arc was nearly 0°. With this geometry, the equivalent true strain imparted to the material after one ECAP pass was 1.15. A very low back pressure of 15 MPa was applied just to prevent sliding between the two components of the hybrid. This back pressure had a function similar to welding layers together at the edges to prevent slippage in the ARB process. The ECAP processing temperature of 175°C was chosen to avoid the occurrence of strain-induced martensitic transformation [48].

With the increasing number of ECAP passes, strain was accumulated and a greater degree of grain refinement was expected. Two main variables viz. the geometry factor (the diameter of the steel core and the thickness of the cladding AA6201 layer, or core/rod diameter ratios) and the number of ECAP passes were chosen in this study. Altogether, six types of bimetallic structures (with three different geometries and two kinds of processing history) were manufactured. The microstructure evolution and the properties of the AA6201 rod in isolation, rather than within a bimetallic rod, were also considered in order to

Table 1 Chemical composition of stainless steel 316 L and AA6201 in wt%

Steel 316L	Fe	C	Mn	Ni	Cr	Mo	Si	Cu	S	P	V
	Bal	0.02	1.51	10.0	16.6	2.09	0.38	0.43	0.02	0.04	0.05
AA6201	Al	Si	Mg	Cu	Fe	Zn	Cr	Ni	Mn	Ti	
	Bal	0.56	0.73	0.13	0.31	0.13	0.01	0.01	0.14	0.01	

evaluate the effect of co-deformation of the two constituents of the hybrid rods.

Electrical conductivity measurements

The SIGMATEST Ec device (Foerster Instruments Inc., Pittsburgh, USA) was used to determine the electrical conductivity of the samples. This equipment operates on the basis of the eddy-current method. Since the size and shape of the tested samples can affect the measurement, all tested samples had the same cylinder geometry with 10 mm height and 10 mm diameter. They were cut from the middle of the billets. Each sample was tested 10 times to calculate the average value of the electrical conductivity.

Mechanical properties

Due to the difficulties of making tensile test samples from bimetallic rods, tensile test was not practicable. Instead, compression tests were carried out to evaluate the mechanical properties using an Instron 5982 machine. The compression samples were cut from the middle of the billets with 10 mm height and 10 mm diameter. The cross-head velocity was set to

0.01 mm/s to provide a nominal strain rate of 10^{-3} s^{-1}.

Microstructure characterisation

Low-magnification overviews of the sample cross-sections were obtained using Olympus SZX-16 stereo optical microscope equipped with a digital camera. X-ray diffraction (XRD) measurements were performed using a Philips X-ray diffractometer with Cu Kα radiation at 40 kV and 25 mA. Data were processed using the peak fitting program MDI Jade for accurate computation. Transmission electron microscopy (TEM) characterisation was performed using a FEI Tecnai F20 FEG TEM operating at an acceleration voltage of 200 kV. The TEM foils were prepared by focused ion beam (FIB) lift-out using a FEI Quanta FEG SEM.

Results

Optical microscopy observation

From the optical micrographs shown in Fig. 1, it is clearly seen that after a single ECAP pass the shape of

Figure 1 Optical microscopy images of the cross-sections showing the shape transformation of the steel cores after one and four ECAP passes: **a**–**c** initial shapes of samples with three different core diameters (before ECAP, denoted 0p), **d**–**e** after one ECAP pass (denoted 1p), **g**–**i** after four ECAP passes (denoted 4p).
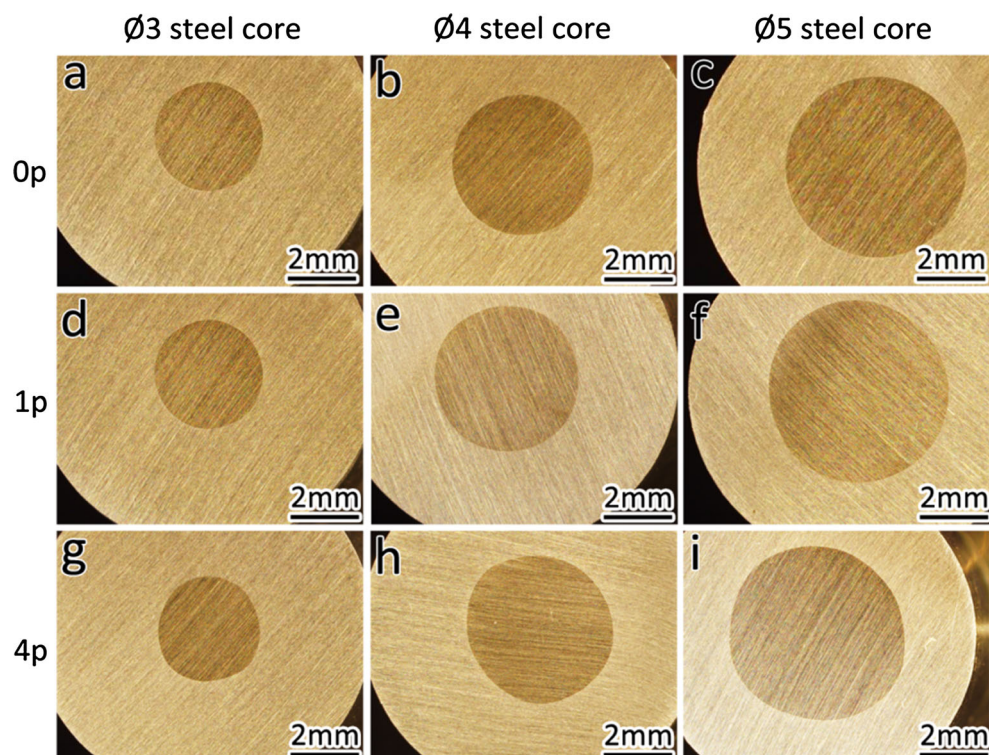
steel cores changed from a perfect circle to a more irregular one and after four passes, the core shape was distorted even stronger. This observation indicates that co-deformation of the steel core took place and that the amount of strain increased with higher number of ECAP passes. Furthermore, from the observation of the cross-sections, no delamination at the interfaces between the two components of a hybrid structure was detected after ECAP processing.

Measurements of mechanical properties

To evaluate the impact of the co-deformation induced by ECAP on the mechanical strength of bimetallic rods, compression tests were carried out. The stress in bimetallic rods was determined as the overall axial load divided by the initial cross-sectional area of the hybrid rod. The values of the compressive yield strength of the tested materials at 0.2 % offset strain are listed in Table 2. It can be seen that, in the initial condition, bimetallic rods exhibited a slightly higher strength than AA6201 rod, the difference being in the range from 25 to 50 MPa, depending on the diameter of the steel core. In other words, the steel core did not bring much strengthening to the bimetallic rod. However, after four ECAP passes, the difference increased and varied from 50 to 100 MPa. For bimetallic rod with Ø3 and Ø4 steel core, the increment mostly occurred after the first ECAP pass, from 300 and 306 MPa to 390 and 418 MPa, respectively.

However, further increase in the yield strength with the number of ECAP passes is evident.

Measurements of electrical conductivities

The electrical conductivity results are shown in Table 3. It is seen that with increasing number of ECAP passes, the electrical conductivity of stand-alone AA6201 and steel 316L decreases slightly due to the deformation-induced crystal lattice defects that scatter electrons [44, 49]. This is at variance with the results of the work conducted by Valiev et al. [44], who demonstrated that after processing by high-pressure torsion (about 20 revolutions) of a solution-treated AA6201, both strength and electrical conductivity increased to values exceeding those for the peak-aged AA6201. In their tests, the deformation corresponded to an equivalent strain of 483 according to the equation $\varepsilon_{\text{eff}} = N \cdot 2\pi r / t\sqrt{3}$, where r is the distance from the axis (up to 10 mm), t is the thickness of the sample (1.5 mm), and N is the number of revolutions [50]. In contrast, in the present study, 4 ECAP passes imposed a much lower equivalent strain of 4.6, which was apparently not high enough for improving electrical conductivity to the same extent in the stand-alone AA6201 rod. Similarly, in the case of bimetallic rods with Ø4 and Ø5 steel core, samples in the initial condition exhibited a higher electrical conductivity than those with an ECAP processing history.

Table 2 Compressive yield strength at 0.2 % offset of AA6201 rod and bimetallic rods with three geometries after 0, 1 and 4 ECAP passes (in MPa)

Number of ECAP passes	Yield strength of AA6201 rod	Yield strength of bimetallic rod with Ø3 steel core	Yield strength of bimetallic rod with Ø4 steel core	Yield strength of bimetallic rod with Ø5 steel core
0	274	300	306	325
1	323	390	418	492
4	380	424	449	590

Table 3 Electrical conductivity of AA6201 rod, steel rod and bimetallic rod with three geometries after 0, 1 and 4 ECAP passes (in IACS %)

Number of ECAP passes	Conductivity of AA6201 rod Ø10	Conductivity of bimetallic rod with Ø3 steel core	Conductivity of bimetallic rod with Ø4 steel core	Conductivity of bimetallic rod with Ø5 steel core	Conductivity of steel rod Ø10
0	47.23 ± 0.13	42.37 ± 0.98	37.40 ± 0.85	25.51 ± 0.48	2.26 ± 0.01
1	46.59 ± 0.26	42.79 ± 0.34	34.49 ± 1.05	21.83 ± 0.53	2.25 ± 0.01
4	46.36 ± 0.13	43.19 ± 0.43	34.69 ± 0.36	23.78 ± 0.35	2.19 ± 0.02

However, for the bimetallic rod with Ø3 steel core, ECAP brought about a slight increase of the average conductivity from 42.37 % IACS to 42.79 % IACS and 43.19 % IACS after one and four ECAP passes, respectively. Although the increments are within the scatter of the measurements, it is evident that the magnitude of the electrical conductivity was maintained. Combining the results from the compression test, this suggests that for the bimetallic rod with Ø3 steel core, ECAP processing gave rise to a higher yield strength over that of the initial rod. This was not accompanied with a loss of the electrical conductivity. In other words, it can be concluded that the usual trend of an inverse relation between electrical conductivity and strength was confirmed for AA6201 rod. By contrast, for bimetallic rod, it was possible to reverse this trend: as a result of ECAP processing, strength was enhanced without a loss of electrical conductivity.

To get a better insight into the influence of the ECAP processing history and the geometry factor on the overall performance of the bimetallic rod, the electrical conductivity and yield strength results are plotted together in Fig. 2. Three hybrid geometries are represented in terms of the volume fraction of the steel core in the bimetallic structure. For the bimetallic rods with Ø3, Ø4 and Ø5 steel core, these volume fractions are, respectively, 9, 16 and 25 %. The dashed black line in the figure corresponds to the yield strength of bimetallic rods (calculated on the basis of a linear rule-of-mixture) in the initial non-
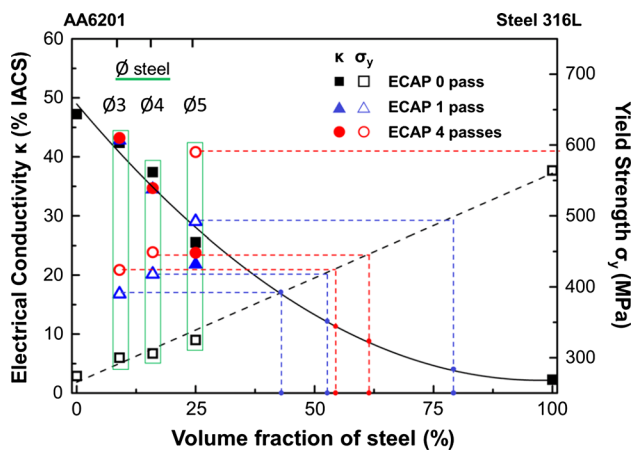
ECAP condition. The solid black line represents a decrease of the electrical conductivity with increasing volume fraction of steel core. We can employ the steel volume fraction dependence of yield strength of non-processed bimetallic rods as represented by the mentioned dashed line to assess the benefits of ECAP processing. Indeed, making use of that curve, one can see that after one ECAP pass the yield strength of bimetallic rods with 9, 16 and 25 % volume fraction of steel is equivalent to the yield strength of unprocessed bimetallic rods with approximately 40, 52 and 78 % volume fraction of steel, respectively, cf. the blue dashed lines. Similarly, after four passes, the yield strength of the bimetallic rods is equivalent to that of unprocessed bimetallic rods with approximately 54, 60 and 100 % volume fraction of steel, respectively, cf. the red dashed lines. That is to say, through processing by ECAP, a bimetallic rod with a thinner steel core can maintain the same level of yield strength as an unprocessed bimetallic rod with a thicker one, while the electrical conductivity of the former will be greater due to the larger volume fraction of aluminium it has. Comparing bimetallic rods that are equivalent in terms of yield strength—390, 418 and 492 MPa, it can be seen that the electrical conductivity of 17, 13 and 4 % IACS (indicated by the blue points on the solid black line) rises to 43, 34 and 22 % IACS after one ECAP pass, respectively, due to the increased volume fractions of AA6201 component. In the same way, for bimetallic rods with the yield strength of 424, 449 and 590 MPa, the electrical conductivity of unprocessed rods rises from 12, 8 and 2 % IACS (see the red points on the solid black line) to 43, 35 and 24 % IACS after four ECAP passes, respectively.

The result can be interpreted as follows. Through ECAP processing, one can attain a certain level of strength of Al clad steel rod or wire with a thinner steel core. This means a lighter product with a higher specific strength and, for certain core/rod diameter ratios, a higher electrical conductivity.

XRD characterisation

XRD analysis was conducted on all 12 samples prepared. The XRD spectra of bimetallic rod with Ø5 steel core after 0, 1 and 4 ECAP passes are presented in Fig. 3. Phase identification failed to detect any martensite after 4 ECAP passes, which means that either martensitic transformation did not occur in the

Figure 2 Electrical conductivity and yield strength of as-received Ø10 AA6201 and steel rods and bimetallic rods with three different geometries (Ø3, Ø4, and Ø5 steel core) after 0, 1 and 4 ECAP passes.

Figure 3 X-ray diffraction patterns of bimetallic rods with Ø5 steel core after 0, 1 and 4 ECAP passes.

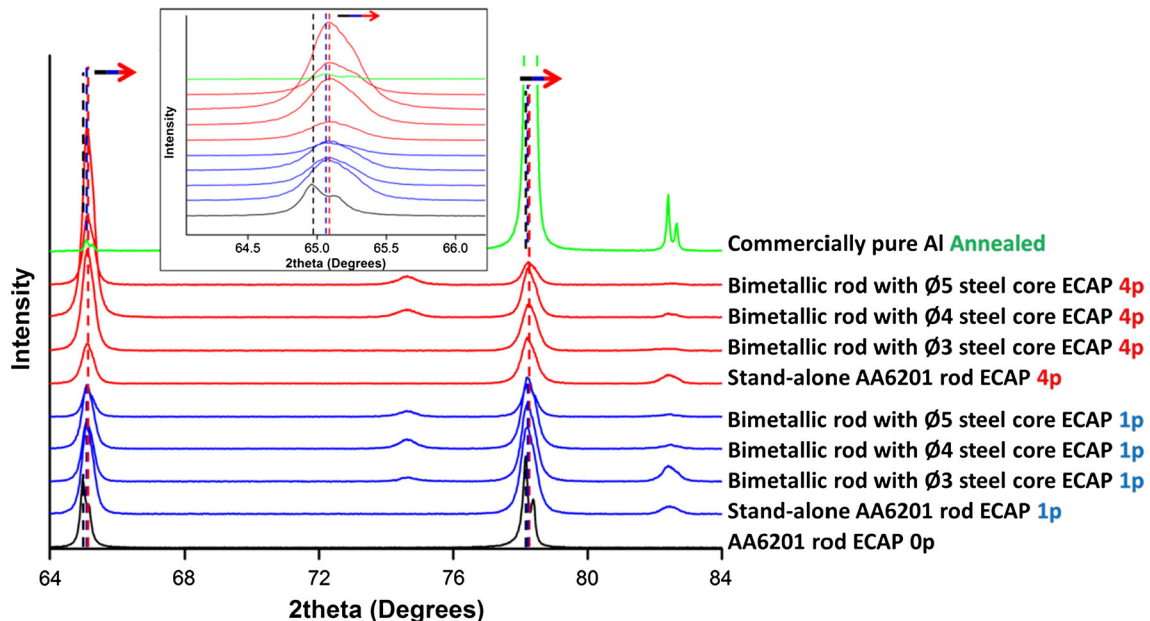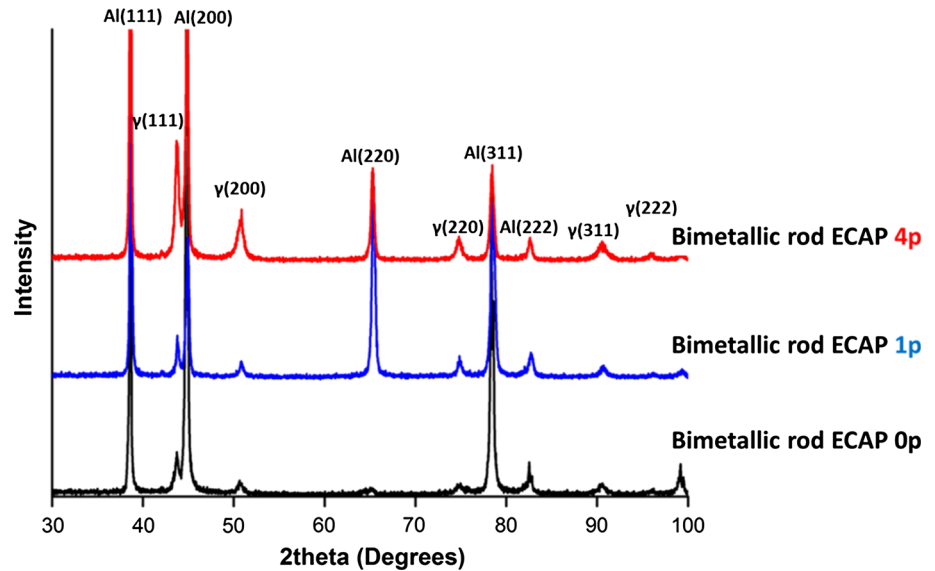**Figure 4** X-ray diffraction patterns of stand-alone AA6201 and bimetallic rods with three different geometries (Ø3, Ø4 and Ø5 steel core) after 0, 1 and 4 ECAP passes. The *inset* shows an enlarged view of peak (311). Well annealed commercially pure Al was used as a reference material.

first place or the amount of martensite formed was below the detection limit of XRD. At any rate, it can be stated safely that ECAP processing did not introduce a significant amount of martensite. From XRD data, the lattice parameter of AA6201 constituent was calculated by determining the positions of diffraction peaks. In this study, peaks for (220), (311) and (222) reflections were chosen as shown in Fig. 4. Since the calculated lattice parameter is significantly affected

by the diffraction angle θ, the error in the calculated magnitude $\sin\theta$ being smaller for larger θ values, the (111) and (200) diffraction peaks were not included. The lattice microstrain, the crystalline size and the dislocation density were determined by measuring peak broadening, as detailed in Refs. [51–53]. XRD peak profiles were fitted using the Pearson VII function with K-alpha2 present, and the full-width at half-maximum (FWHM) of peaks was obtained as a

Table 4 Microstructural characteristics of AA6201 rod and the AA6201 constituents of bimetallic rods after one and four ECAP passes

Al in	ECAP passes	Lattice parameter (Å)	Crystallite size (nm)	Lattice microstrain	Dislocation density (m^{-2})
Al annealed	0p	4.0502	–	–	–
AA6201 rod Ø10	0p	4.0550	–	–	–
	1p	4.0524	462	0.0025	6.5×10^{13}
	4p	4.0517	231	0.0029	1.5×10^{14}
Bimetallic rod with steel core Ø3	1p	4.0520	231	0.0031	1.6×10^{14}
	4p	4.0505	198	0.0029	1.8×10^{14}
Bimetallic rod with steel core Ø4	1p	4.0515	198	0.0033	2.0×10^{14}
	4p	4.0513	115	0.0027	2.8×10^{14}
Bimetallic rod with steel core Ø5	1p	4.0516	115	0.0033	3.4×10^{14}
	4p	4.0505	126	0.0031	3.0×10^{14}

measure of peak broadening. The instrumental broadening was determined using a well annealed (400 °C for 4 h) commercially pure Al sample. The true peak broadening B was calculated using $B = \sqrt{B_{obs}^2 - B_{inst}^2}$, where B_{obs} is the observed peak and B_{inst} is the instrumental broadening one [54].

As seen from Fig. 4, in which the diffraction patterns for the AA6201 constituent after 0, 1 and 4 ECAP passes are juxtaposed, there is a clear shift of (220) and (311) peaks for Al phase to greater diffraction angles, which reveals a decrease of the lattice parameter [55]. It is also worth noting that the decrease of the lattice parameter of AA6201 cladding layers was greater than that of the stand-alone AA6201 rods. The characteristics of stand-alone AA6201 and the AA6201 constituents of the bimetallic rods determined from the peak shift and peak broadening are presented in Table 4. It is seen that AA6201 has the largest lattice parameter of 4.0550 Å. With severe plastic deformation imposed on the stand-alone AA6201 at 175 °C, this value dropped to 4.0524 Å and 4.0517 Å, indicating a decomposition of the AA6201 solid solution matrix by dynamic ageing. However, apparently the extent of depletion of solid solution was not large enough to compensate for the contribution of deformation-induced lattice defects to electron scattering. Therefore, the electrical conductivity still decreased even with less solute atoms in solid solution. The AA6201 component in bimetallic rods exhibits the same trend of decreasing lattice parameter with the increasing amount of plastic strain imparted to the rod. However, by comparing the magnitudes of the lattice parameter in a stand-alone AA6201 rod and AA6201/steel bimetallic rod, it can be found that with the steel core embedded, the extent of decomposition of the AA6201 bulk is even higher. After one and four EACP passes, the magnitudes of the lattice parameter of AA6201 component in bimetallic rods were 4.0515–4.0520 Å and 4.0505–4.0513 Å. These values are smaller than the above figures for the stand-alone AA6201. This indicates that having steel core co-deformed with the AA6201 sheath can promote the dynamic ageing thus leading to the formation of secondary precipitate phases and the concomitant depletion of solid solution. This is obviously a desired scenario, as the precipitates formed do not contribute to electron scattering significantly, while the reduction of the concentration of alloying atoms in solid solution decreases the density of scattering centres and promotes better electrical conductivity. A decrease of the lattice parameter signifies a drop in the solute concentration.

The dislocation density in the AA6201 rod showed an almost two-fold increase, from 6.5×10^{13} m^{-2} after the first ECAP pass to 1.5×10^{14} m^{-2} after the fourth one. However, in the AA6201 component in bimetallic rods, the dislocation density jumped from 1.6×10^{14} to 3.4×10^{14} m^{-2}, after just one pass of ECAP. It remained pretty steady and was in the range of 1.8×10^{14} to 3.0×10^{14} m^{-2} after the fourth ECAP pass. The crystallite size also evolved as a result of ECAP processing: after four passes, the average crystallite size of stand-alone AA6201 rod decreased to 231 nm, which is comparable with the values reported in [56, 57]. The AA6201 component in

bimetallic configuration exhibited an average crystallite size that approached saturation after just one ECAP pass, with characteristic values down to 115 nm.

TEM characterisation

Based on the results presented above, three bimetallic rods were chosen for further characterisation by TEM. FIB lift-out was employed to cut TEM lamellas from the interface regions between the AA6201 cladding layer and the steel core. Figures 5, 6, 7 show that the microstructure varied significantly with increasing imposed strain and different core/rod diameter ratios. The influence of the number of ECAP passes can be seen from Figs. 5 and 6 that refer to samples with the same core diameter of Ø3 but different amount of imposed equivalent strain, 1.15 or 4.6 (one or four passes, respectively). Figures 6 and 7 provide a comparison between the microstructures for the same processing history (four ECAP passes), but different core diameters (Ø3 and Ø5 steel core).

An overview of an interface between AA6201 and steel components of a bimetallic rod with Ø3 steel core after one ECAP pass is shown in a bright-field (BF) TEM image in Fig. 5a. It can be seen that these two components were tightly joined without obvious gap between them. However, a closer inspection of Fig. 5c reveals an elongated void along the interface 40 nm in width. To the left side of the interface, an interfacial Al layer that underwent profuse plastic flow is observed; it is highlighted by a read-dashed circle. Because AA6201 is softer than austenitic steel 316L, it is believed to accommodate a larger amount of plastic strain by the intensive plastic flow at the interface. Obviously, the material on the steel side accumulated a large strain, as well. As seen in Fig. 5d, next to the interface, there is an area with subgrain structures having the size smaller than 50 nm. Farther away from the interface, grain structures change to micro size, with extended boundaries inclined to the pressing direction (henceforth referred to as extrusion direction, ED), as indicated by the yellow dashed lines in Fig. 5a, d. In the AA6201 component, grains are equiaxed, as shown in Fig. 5a, b. The average grain size was calculated by averaging over 100 grains to be 224 ± 103 nm, which is close to the value of 231 nm obtained by XRD analysis.

TEM-BF images in Fig. 6 demonstrate that a larger amount of imposed strain after four ECAP passes altered the interface microstructures in a number of ways. First, comparing with a lesser strain after the first pass, the extremely deformed zone got larger with three more passes, cf. Figure 6a. It can be seen
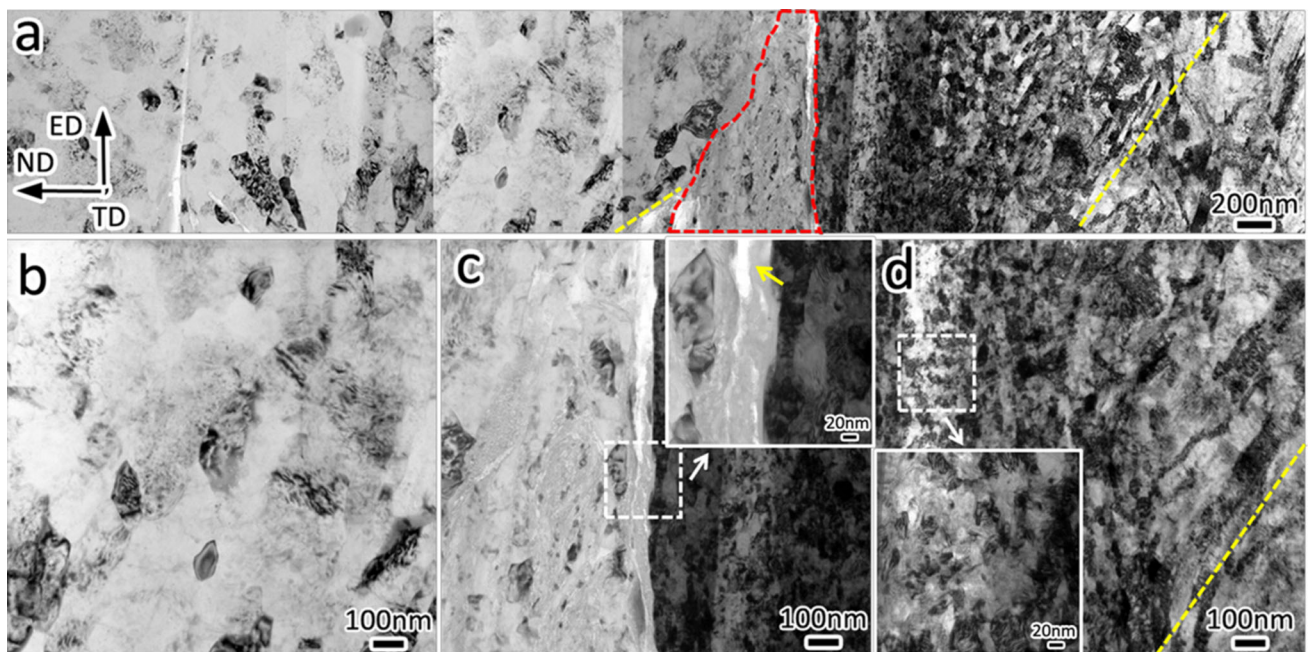

Figure 5 TEM-BF images of **a** the interface between AA6201 (*left*) and steel (*right*) from bimetallic rod with Ø3 steel core after one ECAP pass, **b** AA6201, **c** interface, and **d** steel with high magnification. *Insets* are enlarged views of the areas indicated by *arrows*.
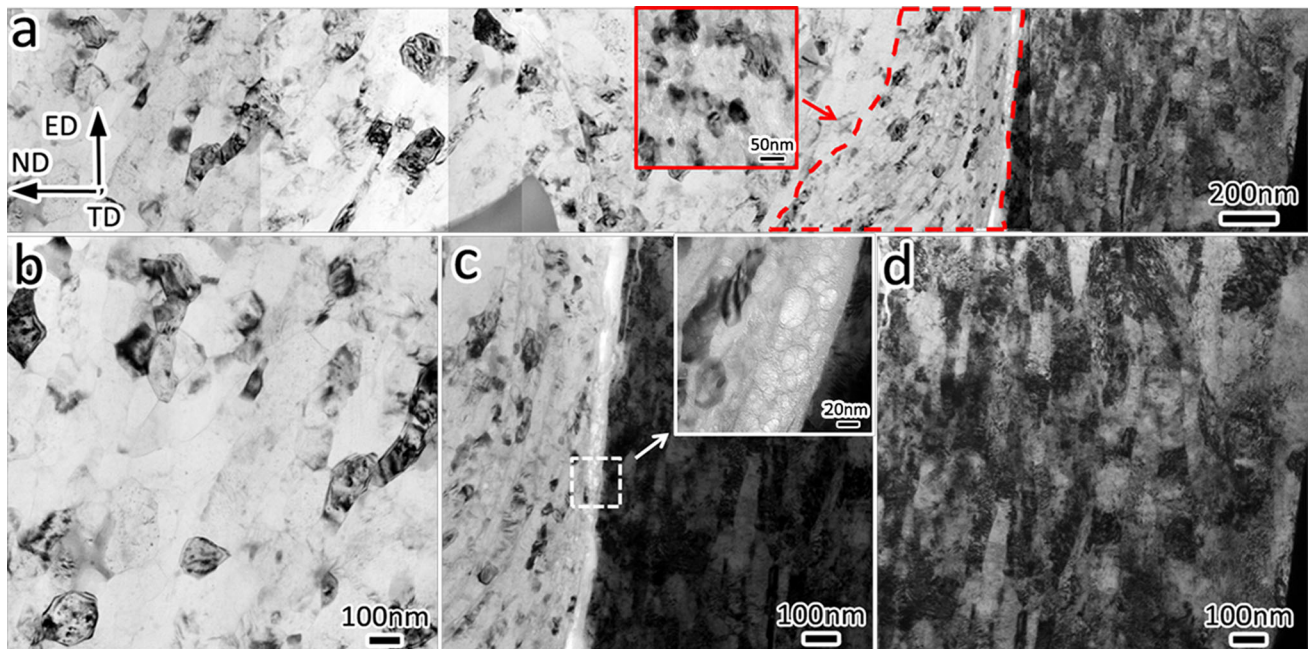
Figure 6 TEM-BF images of **a** the interface between AA6201 (*left*) and steel (*right*) from bimetallic rod with Ø3 steel core after four ECAP passes, **b** AA6201, **c** interface, and **d** steel with high magnification. *Insets* are enlarged views of the areas indicated by *arrows*.

from the inset that the scale of the subgrain structure is around 50 nm. Second, the interface between AA6201 and steel in Fig. 6c shows that both components are tightly bonded. An amorphous layer, about 60 nm thick, was detected. Third, in the case of steel component, the extra three ECAP passes did not bring about any further grain refinement. On the contrary, the grains were coarsened and got elongated in the extrusion direction as shown in Fig. 6a, d. In essence, the microstructure of the steel core evolved from a nano/submicron-sized subgrain pattern inclined to the extrusion direction to an ultrafine grain structure, with grains aligned in the extrusion direction, as seen in Fig. 6d. This is believed to be a consequence of dynamic recrystallisation, the recrystallised grain structure consuming the subgrain structure developed after the first pass. Finally, in Fig. 6b, equiaxed grains without any preferred orientation were predominant in the AA6201 component of the bimetallic rod. The grain size determined by averaging over 100 grains was 200 ± 85 nm, a figure that is very close to that obtained by XRD analysis (198 nm).

TEM images of bimetallic rod with Ø5 steel core (the largest diameter of steel core and the thinnest AA6201 cladding layer) after 4 ECAP passes, i.e. for the same amount of imposed strain as in Fig. 6, is shown in Fig. 7. The most prominent features in

Fig. 7a are fragments of the amorphous layer at the interface indicated by arrows. In an enlarged view in Fig. 7c, they appear to be caused by a shear instability and a displacement of the two components at the interface relative to each other. Plastic instability at the interface is documented by the occurrence of shear banding in the steel phase shown in Fig. 7a, d. The inset in Fig. 7c shows that AA6201 and steel interpenetrated each other at the interface and formed a mechanical interlocking between the mating surfaces. Shear banding in the steel component is likely to be related to this process as a way to accommodate the severe plastic strain in bimetallic co-deformation. In addition, it can be seen that steel grains have well-defined grain boundaries in contrast to the subgrain structures in the lower strain case (one ECAP pass) case in Fig. 5d. Alignment of the grains in the extrusion direction is also visible, although they are less elongated than in bimetallic rod with a smaller steel core presented in Fig. 6d. Finally, back to the AA6201 component in Fig. 7b, it can be seen that grains are equiaxed, with the average grain size of 130 ± 49 nm, in accord with the value obtained by XRD (126 nm).

A close-up picture of the grain structure in steel after ECAP processing is presented in Fig. 8. With an average grain size of 65 ± 20 nm, the material can be classified as nanostructured. No martensite was
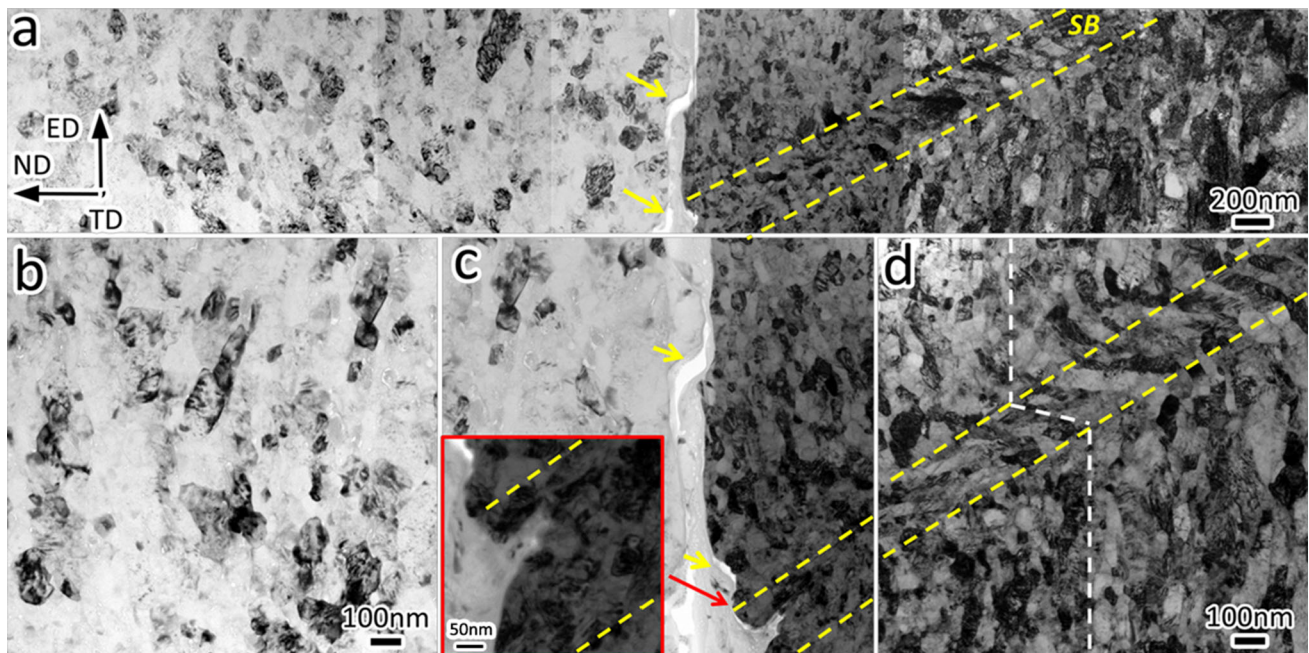
Figure 7 TEM-BF images of **a** the interface between AA6201 (*left*) and steel (*right*) from bimetallic rod with Ø5 steel core after four ECAP passes, **b** AA6201, **c** interface and **d** steel with high magnification. A pair of *dashed lines* delineate a shear band (SB).
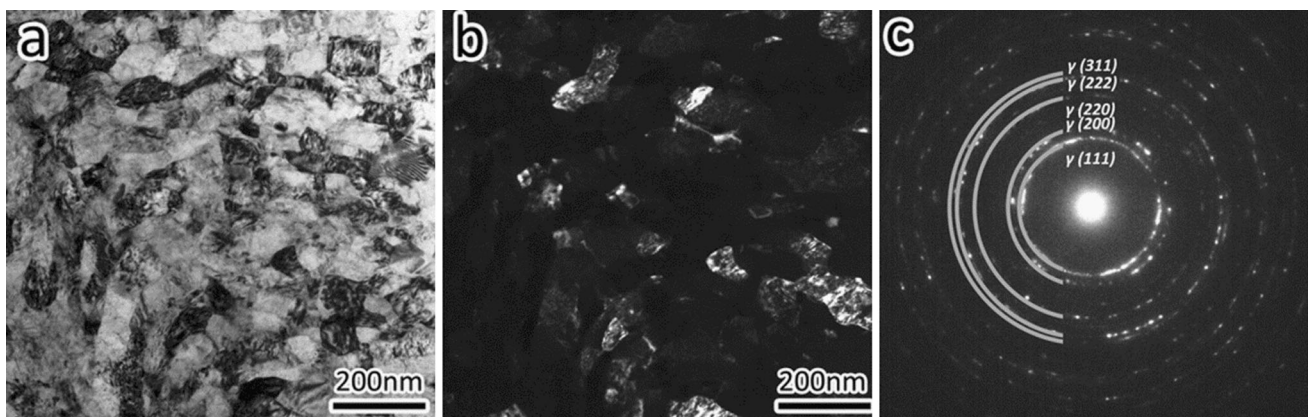

Figure 8 TEM images of Ø5 steel core subjected to four ECAP passes with **a** bright-field image, **b** dark-field image and **c** the corresponding SADP obtained using aperture diameter of 0.75 μm.

detected by selected area diffraction pattern (SADP). A continuous ring pattern suggests a random grain orientation and the occurrence of a large fraction of high-angle grain boundaries (HAGBs) in this region. This again confirms the XRD phase identification results showing that no phase transformation occurred during ECAP processing.

TEM characterisation was used to image precipitates in AA6201 grains. As shown in Fig. 9a, the as-received

AA6201-contained needle-shaped metastable β″ precipitates on [001] planes. After one ECAP pass at 175°C, no needle-shaped precipitates were observed and dislocation cells were present, as seen in one grain in Fig. 9 (b). This suggests that solute atoms in solid solution and dislocations contributed to a decrease of conductivity. After three more ECAP passes dislocation, cell boundaries were transferred to grain boundaries and few nano-sized second-phase precipitates were developed,
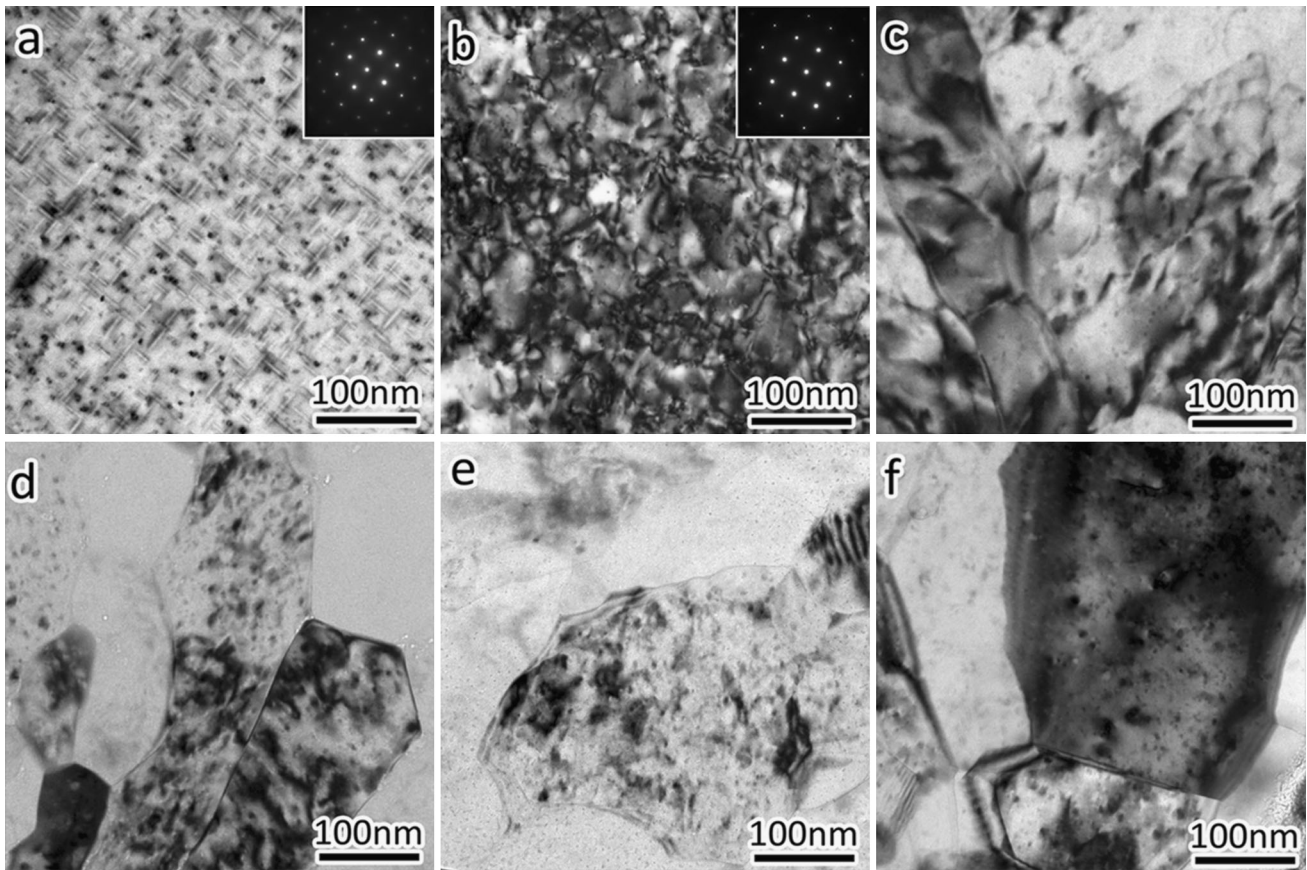
Figure 9 TEM-BF images showing AA6201 grain(s) from **a** as-received Al alloy with needle-shaped β″ precipitates clearly visible on (001) plane, **b**, **c** stand-alone Al after one and four ECAP passes, **d**, **e** AA6201 component in bimetallic rod with Ø3 steel core after one and four ECAP passes, **f** AA6201 component in bimetallic rod with Ø5 steel core after four ECAP passes. Note that **a**, **b** were taken normally to <001> zone axis, whereas, due to the strong diffraction contrast, **c**–**f** were not taken on zone axis. The occurrence of strain contours in some of the images should be noted.

Figure 10 Schematic illustration of frictional shear stresses acting on the AA6201 cladding layer during ECAP deformation and the intersection angles of steel and AA6201 layer.
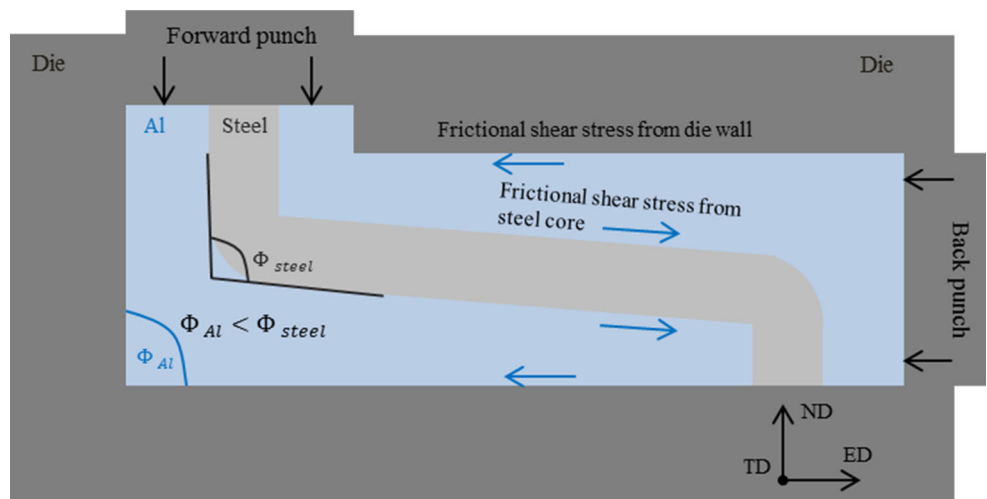
cf. Figure 9c. By contrast, Fig. 9d shows that the AA6201 component that went through just one ECAP pass, but with a Ø3 steel core embedded, had a developed fine grain structure with well-defined grain boundaries. Solute aggregate nanostructures are also observed here. In this case, the combination of these microstructural

features led to a slight increase of electrical conductivity. With higher imposed strain, a large number of spherical-shaped solute aggregate nanostructures are observed, cf. Figure 9e, f, which have similar morphology to those in Refs. [44, 58, 59]. All these features contribute to raising the electrical conductivity.

The dynamic ageing of 6xxx series Al alloys under severe plastic deformation has been studied by a number of groups. The main finding is that the severe plastic deformation can cause fragmentation of metastable β' phase into several parts with spherical shape [60]. With increasing amount of plastic deformation, they grow to nano-sized solute aggregates, which process is accompanied with a depletion of solid solution [44]. The high density of ECAP-induced crystal lattice defects such as vacancies and dislocations can increase the diffusivity of solutes in a very significant way, thus accelerating dynamic ageing [57, 59–61]. Based on this knowledge, it can be summarised that, due to load sharing between the steel core and the AA6201 cladding, ECAP processing can provide a strain on the cladding layer sufficient to achieve effective dynamic ageing, therefore 'purify' the bulk through formation of nano-scale solute clusters analogous to what was found for HPT processing [44]. This is at variance with the case of stand-alone AA6201, in which the strain provided by ECAP was insufficient to induce effective dynamic ageing and decomposition of solid solution.

Discussion

From the quantitative analysis by XRD and TEM conducted in this study, it can be seen that, under the same processing conditions, the AA6201 component of the hybrid material with an embedded steel core went through more efficient dynamic recrystallisation (as revealed by the smaller average grain size and the morphology of the grains) and dynamic ageing (as reflected in the magnitude of the lattice parameter) than stand-alone AA6201. In addition, by comparing different hybrid materials, it was found that the geometry of the rod, i.e. the core/rod diameter ratio, has a strong influence on the interface bonding. These phenomena lead us to discuss the co-deformation mechanism. By analogy with the co-deformation mechanism that has been considered for extrusion [62], spiral extrusion [63] and accumulative roll bonding [64], the microstructure evolution in the

current system can be associated with friction between the AA6201 cladding layer and the die wall on its outer surface and the steel core on its inner surface.

A schematic illustration of the friction between the AA6201 cladding layer and the die wall and the steel core is shown in Fig. 10. It is seen that during ECAP deformation, the die wall causes a frictional shear stress in the AA6201 layer acting in the direction opposite to the extrusion direction. With the steel core having a higher flow velocity, there is also a friction shear stress acting in the extrusion direction at the interface between AA6201 and steel. The flow velocity difference between the regions near the outer surface of the rod and the interface decreases with increasing cladding layer thickness. This phenomenon was also found in extrusion process [62]. Due to a smaller distance between the two friction surfaces, a thinner cladding layer would be experiencing a higher level of shear stress, which is consistent with a more pronounced grain refinement in this case, as observed experimentally, cf. Figs. 6b and 7b. Furthermore, in the case of thicker cladding layer, with smaller flow velocity difference between the core and the cladding layer, better interface bonding properties are expected, cf. Figs. 6c and 7c.

Another feature that is worth noting in Fig. 10 is the intersection angle of the steel core. It was shown by the observations of the longitudinal sections of a bimetallic rod with hard core and soft cladding layer after ECAP deformation that in practice the intersection angle of the hard core, Φ, is effectively increased [65]. Therefore, the steel core accommodated less effective strain than 1.15 [65]. With thicker AA6201 cladding layer and smaller diameter of the steel core, the intersection angle of steel, Φ_{steel}, is expected to be larger than the one for a larger steel core diameter. That is why for a thicker AA6201 cladding layer, the grain refinement within the steel core is limited (as seen in Fig. 6d), as compared to the very fine grain structure observed in Fig. 7d for a thin AA6201 layer. Also, the occurrence of a shear band in the steel core of 5 mm diameter is a sign that strain accommodation therein was reaching its limits, plastic instability setting in.

In addition, plastic deformation near the interface depends on the inherent mechanical properties of the two materials involved. Aluminium as the softer component accommodates more plastic strain than steel. Differences in the plastic strain in the core and

sheath parts of a bimetallic rod ('plastic incompatibility') also lead to internal stresses acting in different directions in the two constituents. According to Mughrabi's model [66, 67], the back stress in softer AA6201 sheath leads to an increase of the local stress, thus additionally promoting grain refinement there. Conversely, a forward stress acting in the steel core effectively softens it. These effects become less significant for thinner cores, which is consistent with a less pronounced grain refinement in the AA6201 sheath for smaller steel core diameter.

Conclusions

AA6201/316L steel bimetallic rods were successfully produced using ECAP. This technique has the potential to be scaled up for the application in overhead transmission lines. Bimetallic rods with different geometry factors of the steel core and Al cladding produced in this way were investigated. It was found that, beside the sound interface after processing, ECAP can significantly improve the mechanical performance of the hybrid rods. Moreover, among the three variants considered, one kind of geometry viz. a bimetallic rod with a steel core of 3 mm in diameter and Al sheath 3.5 mm in thickness exhibited an outstanding performance in terms of increase of mechanical strength without loss of electrical conductivity after ECAP processing.

It was found that an embedded steel core can promote the dynamic recrystallisation and dynamic ageing processes in AA6201 cladding components. The working hypothesis is that under co-deformation by ECAP, the Al sheath accommodates a greater plastic strain than a mono-material rod under the same processing condition. In addition, the friction shear stress provided by the steel core also contributes to development of favourable microstructure. Thus, on top of simple shear and hydrostatic pressure imparted to the material in the ECAP process, friction shear stress between the cladding layer and the core also influences the interface properties and the local microstructure evolution near the interface. More specifically, having larger hard core material and a thinner cladding layer, while keeping the outer diameter of the bimetallic rod unchanged, leads to a more pronounced grain refinement in both constituents of the hybrid structure. A thinner core and a thicker cladding layer contribute to better

interface bonding. An optimum should be sought on the basis of these findings, depending on the targeted levels of strength, electrical conductivity, durability of the rods and cost of production.

Compliance with ethical standards

Conflict of interest The authors declare that they have no conflicts of interest.

References

[1] Ashby M (2013) Designing architectured materials. Scr Mater 68:4–7

[2] Brechet Y, Embury JD (2013) Architectured materials: expanding materials space. Scr Mater 68:1–3

[3] Raabe D, Choi PP, Li Y, Kostka A, Sauvage X, Lecouturier F, Hono K, Kirchheim R, Pippan R, Embury D (2010) Metallic composites processed via extreme deformation: toward the limits of strength in bulk materials. MRS Bull 35:982–991

[4] Bachmaier A, Pippan R (2013) Generation of metallic nanocomposites by severe plastic deformation. Int Mater Rev 58:41–62

[5] Bouaziz O, Kim HS, Estrin Y (2013) Architecturing of metal-based composites with concurrent nanostructuring: a new paradigm of materials design. Adv Eng Mater 15:336–340

[6] Beygelzimer Y, Estrin Y, Kulagin R (2015) Synthesis of hybrid materials by severe plastic deformation: a new paradigm of SPD processing. Adv Eng Mater 17:1853–1861

[7] Sapanathan T, Khoddam S, Zahiri SH, Zarei-Hanzaki A, Ibrahim R (2016) Hybrid metallic composite materials fabricated by sheathed powder compaction. J Mater Sci 51:3118–3124. doi:10.1007/s10853-015-9621-9

[8] Mousavi SA, Sartangi PF (2008) Effect of post-weld heat treatment on the interface microstructure of explosively

welded titanium–stainless steel composite. Mater Sci Eng, A 494:329–336

[9] Han W, Demkowicz MJ, Mara NA, Fu E, Sinha S, Rollett AD, Wang Y, Carpenter JS, Beyerlein IJ, Misra A (2013) Design of radiation tolerant materials via interface engineering. Adv Mater 25:6975–6979

[10] Lu K (2014) Making strong nanomaterials ductile with gradients. Science 345:1455–1456

[11] Wu X, Jiang P, Chen L, Yuan F, Zhu YT (2014) Extraordinary strain hardening by gradient structure. Proc Natl Acad Sci USA 111:7197–7201

[12] Wang Y, Molotnikov A, Diez M, Lapovok R, Kim HE, Wang JT, Estrin Y (2015) Gradient structure produced by three roll planetary milling: numerical simulation and microstructural observations. Mater Sci Eng, A 639:165–172

[13] Zhu K, Vassel A, Brisset F, Lu K, Lu J (2004) Nanostructure formation mechanism of α-titanium using SMAT. Acta Mater 52:4101–4110

[14] Mishra RS, Mahoney MW (2007) Friction stir welding and processing. ASM International

[15] Diez M, Kim HE, Serebryany V, Dobatkin S, Estrin Y (2014) Improving the mechanical properties of pure magnesium by three-roll planetary milling. Mater Sci Eng, A 612:287–292

[16] Toth L, Arzaghi M, Fundenberger J, Beausir B, Bouaziz O, Arruffat-Massion R (2009) Severe plastic deformation of metals by high-pressure tube twisting. Scr Mater 60:175–177

[17] Osakada K, Limb M, Mellor PB (1973) Hydrostatic extrusion of composite rods with hard cores. Int J Mech Sci 15:291–307

[18] Ahmed N (1987) Extrusion of copper clad aluminum wire. J Mech Working Technol 2:19–32

[19] Tokuno H, Ikeda K (1991) Analysis of deformation in extrusion of composite rods. J Mater Process Technol 26:323–335

[20] Alcaraz JL, Gil-Sevillano J (1996) An analysis of the extrusion of bimetallic tubes by numerical simulation. Int J Mech Sci 38:157–173

[21] Kang CG, Jung YJ, Kwon HC (2002) Finite element simulation of die design for hot extrusion process of Al/Cu clad composite and its experimental investigation. J Mater Process Technol 124:49–56

[22] Kazanowski P, Epler ME, Misiolek WZ (2004) Bi-metal rod extrusion—process and product optimization. Mater Sci Eng, A 369:170–180

[23] Rhee KY, Han WY, Park HJ, Kim SS (2004) Fabrication of aluminum/copper clad composite using hot hydrostatic extrusion process and its material characteristics. Mater Sci Eng, A 384:70–76

[24] Gueydan A, Domengès B, Hug E (2014) Study of the intermetallic growth in copper-clad aluminum wires after thermal aging. Intermetallics 50:34–42

[25] Mori K, Bay N, Fratini L, Micari F, Tekkaya AE (2013) Joining by plastic deformation. CIRP Ann-Manuf Techol 62:673–694

[26] Groche P, Wohletz S, Brenneis M, Pabst C, Resch F (2014) Joining by forming—a review on joint mechanisms, applications and future trends. J Mater Process Technol 214:1972–1994

[27] Martinsen K, Hu S, Carlson B (2015) Joining of dissimilar materials. CIRP Ann-Manuf Techn 64:679–699

[28] Divinski SV, Reglitz G, Golovin IS, Peterlechner M, Lapovok R, Estrin Y, Wilde G (2015) Effect of heat treatment on diffusion, internal friction, microstructure and mechanical properties of ultra-fine-grained nickel severely deformed by equal-channel angular pressing. Acta Mater 82:11–21

[29] Sapanathan T, Khoddam S, Zahiri SH, Zarei-Hanzaki A (2014) Strength changes and bonded interface investigations in a spiral extruded aluminum/copper composite. Mater Des 57:306–314

[30] Kocich R, Macháčková A, Kunčická L, Fojtík F (2015) Fabrication and characterization of cold-swaged multilayered Al–Cu clad composites. Mater Des 71:36–47

[31] Kocich R, Kunčická L, Davis CF, Lowe TC, Szurman I, Macháčková A (2016) Deformation behavior of multilayered Al–Cu clad composite during cold-swaging. Mater Des 90:379–388

[32] Eivani AR, Taheri AK (2007) A new method for producing bimetallic rods. Mater Lett 61:4110–4113

[33] Eslami P, Taheri AK (2011) An investigation on diffusion bonding of aluminum to copper using equal channel angular extrusion process. Mater Lett 65:1862–1864

[34] Zebardast M, Taheri AK (2011) The cold welding of copper to aluminum using equal channel angular extrusion (ECAE) process. J Mater Process Technol 211:1034–1043

[35] Jafarlou DM, Zalnezhad E, Ezazi MA, Mardi NA, Hassan MA (2015) The application of equal channel angular pressing to join dissimilar metals, aluminium alloy and steel, using an Ag–Cu–Sn interlayer. Mater Des 87:553–566

[36] Eslami P, Taheri AK, Zebardast M (2013) A comparison between cold-welded and diffusion-bonded Al/Cu bimetallic rods produced by ECAE process. J Mater Eng Perform 22:3014–3023

[37] Narooei K, Taheri AK (2012) Strain field and extrusion load in ECAE process of bi-metal circular cross section. Appl Math Model 36:2128–2141

[38] Lapovok R, Tóth L, Winkler M, Semiatin S (2009) A comparison of continuous SPD processes for improving the mechanical properties of aluminum alloy 6111. J Mater Res 24:459–469

[39] Raab GJ, Valiev RZ, Lowe TC, Zhu YT (2004) Continuous processing of ultrafine grained Al by ECAP–Conform. Mater Sci Eng, A 382:30–34

[40] Kim B, Kim S, Woo B, Lee H, Park J, Jeong Y, Lee M, Ahn S (2005) High tensile nonmagnetic stainless steel wire for overhead electric conductor, low loss overhead electric conductor using the wire, and method of manufacturing the wire and overhead electric conductor. Google Patents

[41] Verhoeven F, Hejcman D, Lagae G, Gogola P (2015) Non-magnetic stainless steel wire as an armouring wire for power cables. Google Patents

[42] Nefzger P, Kaintzyk U, Nolasco JF (2003) Overhead power lines: planning, design, construction. Springer Science & Business Media

[43] Short TA (2014) Electric power distribution handbook. CRC Press

[44] Valiev RZ, Murashkin MY, Sabirov I (2014) A nanostructural design to produce high-strength Al alloys with enhanced electrical conductivity. Scr Mater 76:13–16

[45] Murashkin MY, Sabirov I, Kazykhanov V, Bobruk E, Dubravina A, Valiev RZ (2013) Enhanced mechanical properties and electrical conductivity in ultrafine-grained Al alloy processed via ECAP-PC. J Mater Sci 48:4501–4509. doi:10.1007/s10853-013-7279-8

[46] Cubero-Sesin JM, In H, Arita M, Iwaoka H, Horita Z (2014) High-pressure torsion for fabrication of high-strength and high-electrical conductivity Al micro-wires. J Mater Sci 49:6550–6557. doi:10.1007/s10853-014-8240-1

[47] Murashkin MY, Sabirov I, Sauvage X, Valiev RZ (2016) Nanostructured Al and Cu alloys with superior strength and electrical conductivity. J Mater Sci 51:33–49. doi:10.1007/s10853-015-9354-9

[48] Ueno H, Kakihata K, Kaneko Y, Hashimoto S, Vinogradov A (2011) Enhanced fatigue properties of nanostructured austenitic SUS 316L stainless steel. Acta Mater 59:7060–7069

[49] Rositter PL (2003) The electrical resistivity of metals and alloys. Cambridge University Press, Cambridge

[50] Zhilyaev AP, Langdon TG (2008) Using high-pressure torsion for metal processing: fundamentals and applications. Acta Mater 53:893–979

[51] Williamson G, Smallman R (1956) Dislocation densities in some annealed and cold-worked metals from measurements on the X-ray debye-scherrer spectrum. Philos Mag 1:34–46

[52] Smallman R, Westmacott K (1957) Stacking faults in face-centred cubic metals and alloys. Philos Mag 2:669–683

[53] Zhao YH, Liao XZ, Jin Z, Valiev RZ, Zhu YT (2004) Microstructures and mechanical properties of ultrafine grained 7075 Al alloy processed by ECAP and their evolutions during annealing. Acta Mater 52:4589–4599

[54] Wen H, Topping TD, Isheim D, Seidman DN, Lavernia EJ (2013) Strengthening mechanisms in a high-strength bulk nanostructured Cu–Zn–Al alloy processed via cryomilling and spark plasma sintering. Acta Mater 61:2769–2782

[55] Lubarda V (2003) On the effective lattice parameter of binary alloys. Mech Mater 35:53–68

[56] Veveçka A, Cabibbo M, Langdon TG (2013) A characterization of microstructure and microhardness on longitudinal planes of an Al–Mg–Si alloy processed by ECAP. Mater Charact 84:126–133

[57] Vaseghi M, Taheri AK, Hong SI, Kim HS (2010) Dynamic ageing and the mechanical response of Al–Mg–Si alloy through equal channel angular pressing. Mater Des 31:4076–4082

[58] Roven HJ, Liu M, Werenskiold JC (2008) Dynamic precipitation during severe plastic deformation of an Al–Mg–Si aluminium alloy. Mater Sci Eng, A 483–484:54–58

[59] Sha G, Tugcu K, Liao XZ, Trimby PW, Murashkin MY, Valiev RZ, Ringer SP (2014) Strength, grain refinement and solute nanostructures of an Al–Mg–Si alloy (AA6060) processed by high-pressure torsion. Acta Mater 63:169–179

[60] Tugcu K, Sha G, Liao XZ, Trimby P, Xia JH, Murashkin MY, Xie Y, Valiev RZ, Ringer SP (2012) Enhanced grain refinement of an Al–Mg–Si alloy by high-pressure torsion processing at 100 & #xB0;C. Mater Sci Eng, A 552:415–418

[61] Oh-ishi K, Hashi Y, Sadakata A, Kaneko K, Horita Z, Langdon TG (2002) Microstructural control of an Al–Mg–Si alloy using equal-channel angular pressing. Mater Sci Forum Trans Tech Publ 333–338

[62] Khosravifard A, Ebrahimi R (2010) Investigation of parameters affecting interface strength in Al/Cu clad bimetal rod extrusion process. Mater Des 31:493–499

[63] Sapanathan T, Khoddam S, Zahiri SH (2013) Spiral extrusion of aluminum/copper composite for future manufacturing of hybrid rods: a study of bond strength and interfacial characteristics. J Alloy Compd 571:85–92

[64] Mozaffari A, Manesh HD, Janghorban K (2010) Evaluation of mechanical properties and structure of multilayered Al/Ni composites produced by accumulative roll bonding (ARB) process. J Alloy Compd 489:103–109

[65] Shahmir H, Nili-Ahmadabadi M, Mansouri-Arani M, Langdon TG (2013) The processing of NiTi shape memory alloys by equal-channel angular pressing at room temperature. Mater Sci Eng, A 576:178–184

[66] Mughrabi H (2006) Deformation-induced long-range internal stresses and lattice plane misorientations and the role of geometrically necessary dislocations. Philos Mag 86:4037–4054

[67] Mughrabi H (2006) Dual role of deformation-induced geometrically necessary dislocations with respect to lattice plane misorientations and/or long-range internal stresses. Acta Mater 54:3417–3427